Small Crack Effect on Threshold Stress Intensity K_{TH} for High Strength Steel with Internal Hydrogen

Yukitaka Murakami[1*], Hisao Matsunaga[1, 2, 3], Arezou Abyazi[4], Yoshihiro Fukushima[1, 3]

[1] International Institute for Carbon-Neutral Energy Research (I2CNER), Kyushu University, Fukuoka 819-0395, Japan
[2] Institute of Materials Science and Technology, Fukuoka University, Fukuoka 814-0180, Japan
[3] Department of Mechanical Engineering, Kyushu University, Fukuoka 819-0395, Japan
[4] Department of Materials Engineering, Sahand University of Technology, Tabriz, Iran
* Corresponding author: murakami.yukitaka.600@m.kyushu-u.ac.jp

Abstract   The size effect of the threshold stress intensity K_{TH} for hydrogen-precharged specimens of SAE52100 were investigated. Four types of tensile specimens were used: (i) smooth specimens and (ii) specimens having various shapes of artificial defects with sizes of about 35 ~ 500 μm. In the smooth specimens, fracture origins were nonmetallic inclusions with the size of 10 ~ 30 μm (*e.g.* $Al_2O_3 \cdot (CaO)_x$, TiN and TiC). The fracture toughness determined for the small defects at fracture origin, *i.e.* the K_{TH} calculated from the defect size $\sqrt{area}$ and the fracture tensile stress σ_f, showed a defect size dependence, where, *area* denotes the area of the domain defined by projecting the defect on a plane normal to the cylindrical axis of the specimen. The values of K_{TH} for both the nonmetallic inclusions and artificial defects were much smaller than those for large cracks measured by the standard WOL and CT specimens.

Keywords   Threshold stress intensity, Defect size, Nonmetallic inclusion, Hydrogen embrittlement, High strength steel

1. Introduction

Hydrogen causes degradation of various strength properties, such as tensile strength, ductility, fatigue strength, fracture toughness and *etc*. [1-3] Among them, the fracture toughness such as K_{IC} and J_{IC} is recognized as one of the most important property for the structural integrity of high-pressure hydrogen storage vessels and hydrogen supply systems. Moody *et al.* [4] showed how the fracture toughness K_{TH} of low alloy steels varies with yield strength and hydrogen pressure. Figure 1 schematically shows the relationship between K_{TH} of a steel in hydrogen gas as a function of the yield strength σ_{YS} [1]. Once σ_{YS} exceeds about 1500 MPa, K_{TH} reachs a lower limit between 10 and 20 MPa $\sqrt{\text{m}}$. Similar results on the hydrogen effect on the fracture toughness have been reported also by the other researchers [5 and others].

In most cases, K_{TH} for various materials has been measured for *large cracks* by using standard specimens, *e.g.* WOL and CT. On the other hand, in order to evaluate the effect of small defects on the fracture toughness of high strength steels, Murakami *et al.* [6] carried out a series of tensile tests using hydrogen-precharged (H-precharged) specimens. They determined the K_{TH} values from the fracture stresses and sizes of the nonmetallic inclusions at fracture origins. They reported the followings:

(i) K_{TH} was decreased with an increase in the residual hydrogen content in the material.

(ii) K_{TH} was decreased with a decrease in the defect size. This crack size dependence was similar to that of ΔK_{th} for the small fatigue crack or defect [7, 8].

Above experimental facts caution that the use of the threshold values measured for the *large cracks* leads to an unconservative estimation in the fracture toughness design against *small cracks* or *small defects*. However, the significance of the size effect has not been well recognized despite the presence

of detrimental flows, *e.g.* nonmetallic inclusions and small fatigue cracks, in the real components [9].

In this study, for a more extended understanding of the defect size dependence on the fracture toughness of H-precharged high strength steels, tensile tests of SAE52100 were carried out using specimens having various shapes of artificial surface defect with sizes of about 35 ~ 500 μm. The smooth specimens were also tested to investigate the fracture toughness for subsurface nonmetallic inclusions with sizes of about 10 ~ 30 μm.

2. Experimental

2.1. Material and specimen

Figure 1. Schematic relationship between the threshold stress intensity factor K_{TH} of a steel in hydrogen gas as a function of the yield strength σ_{YS} [4]

A commercial grade SAE52100 bearing steel was used. The chemical composition in mass% is 1.00 C, 0.26 Si, 0.38 Mn, 0.013 P, 0.001 S, 0.10 Cu, 0.08 Ni, 1.40 Cr, 0.03 Mo, 0.0016 Ti, 0.0005 O and bal. Fe. The steel was heat-treated so that he average Vickers hardness, *HV*, measured with a load of 9.8 N had 712.

Figure 2 shows the shape and dimensions of specimen. In some specimens, the following four types of artificial defects with various sizes were introduced onto the specimen surface; (i) a rectangular slit made by the focused ion beam (FIB) technique, (ii) a semi-circular slit made by the electrical discharging, (iii) a drilled hole which has crack-like thin slits made by the FIB technique and (iv) a hole made by the electrical discharging having the FIB slits. Figure 3 shows the shapes and dimensions of the defects, which are designated as Type A ~ D, respectively.

2.2. Hydrogen precharging (H-precharging) and Tensile testing

The specimens were charged with hydrogen by soaking them in an aqueous solution of 20mass % ammonium thiocyanate at 313 K for 48 hours.

Displacement controlled tests were carried out under a crosshead speed V of 1 mm/min corresponding to the strain rate $\dot{\varepsilon}$ of about 6.5×10^{-5} s^{-1} by using a hydraulically-controlled testing machine in ambient air. All the tensile tests were initiated within 2 hours after the charging. The *time after the H-precharging* means the total hold time in ambient air.

2.3. Measurement of hydrogen content

After each tensile test, the residual hydrogen content $C_{H, R}$ in the specimen was measured by the thermal desorption spectroscopy (TDS). Right after the final fracture of the specimen, circular disks of 2.0 mm-thick were sliced from the broken specimen and used for the TDS analysis.

2.4. Characterization of fracture origins and nonmetallic inclusion rating

The size of the defect was represented by the $\sqrt{area}$, where *area* denotes the area of the domain defined by projecting the crack or defect on a plane normal to the cylindrical axis of the specimen [7, 8, 10].
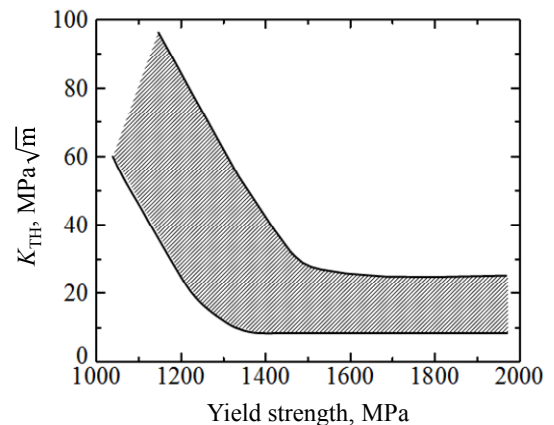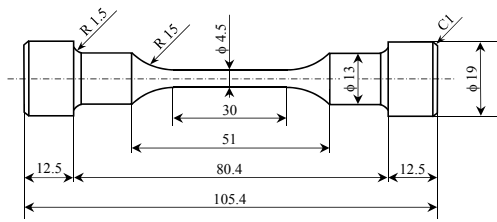
Figure 2. Shape and dimensions of test specimen in mm (Control volume: $V_s =$ 477 mm^3)

(a) Non-metallic inclusion

(b) Artificial defect
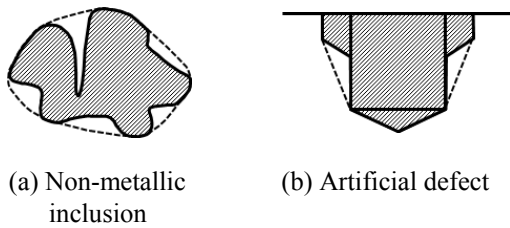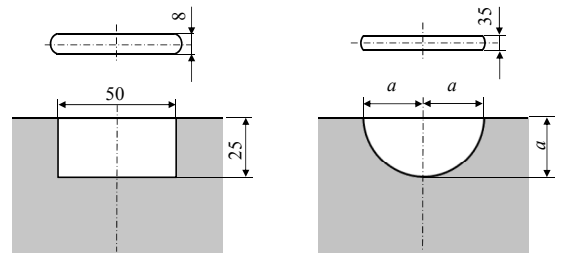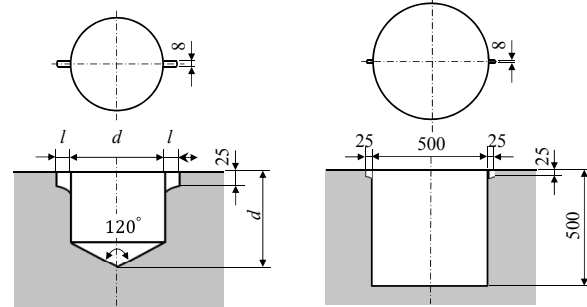
Figure 4. Irregularly shaped defects and estimation method for effective area [8]

(a) Type A: Rectangular FIB slit, $\sqrt{area}$ = 35 μm

(b) Type B: Semi-circular slit made by the electrical discharging, a = 74, 148 or 369 μm, $\sqrt{area}$ = 93.0, 186 or 463 μm

(c) Type C: Drilled hole having crack-like thin slits made by FIB, (d, l) = (100, 50) or (200, 25) μm, $\sqrt{area}$ = 116 or 196 μm

(d) Type D: Electrical discharged hole having crack-like thin slits made by FIB, $\sqrt{area}$ = 513 μm

Figure 3. Shapes and dimensions of artificial defects

The effective area for the defect size $\sqrt{area}$ was estimated by considering a contour which envelopes the original irregular shape of the defect, as shown in Fig. 4 [8].

A newly proposed inclusion rating method [11] based on the statistics of extremes was used.

3. Results and discussion

3.1. Hydrogen content in specimen and the desorption behavior

Figure 5 shows the hydrogen thermal desorption spectra for the H-precharged specimen [12]. Figure 6 displays the residual hydrogen content, $C_{H, R}$, as a function of the total hold time after the charging, Δt, in laboratory air. The content decreased gradually with the hold time. After 100 hours, the content reduced to almost the same level of hydrogen content as in the non-charged specimen. From the reduction of hydrogen content shown in Fig. 6 [12], an apparent hydrogen diffusion coefficient at room temperature, D', was estimated by means of Demarez *et al.'s* solution [13]. The least-square fitting rendered the coefficient to be $D' = 8.6 \times 10^{-13}$ m^2/s. In the H-precharged specimens, all the tensile tests were initiated within 2 hours after the charging, and they were finished within 2 minutes after the initiation of the test; *i.e.* around 4 mass ppm of hydrogen seemed to be present in the specimen during the tensile test.

3.2. Fracture data and fracture origins

Figure 7 shows examples of the uniaxial tension stress-strain curves [12]. All the H-precharged specimens failed at a much lower stress as compared to the non-charged specimens irrespective of the presence or absence of the artificial defect, as shown in Fig. 7, *i.e.* the so-called *hydrogen embrittlement* was demonstrated in the H-precharged specimens. Moreover, the presence of an artificial
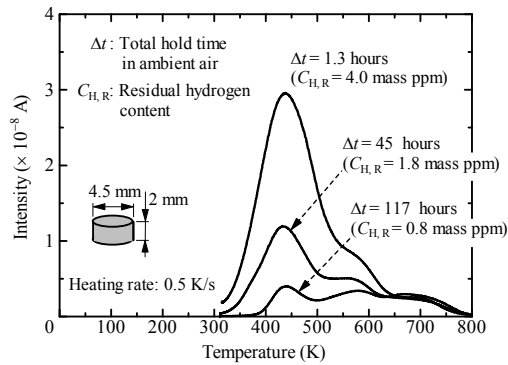
Figure 5. Hydrogen thermal desorption spectra for the hydrogen-charged specimen [12]
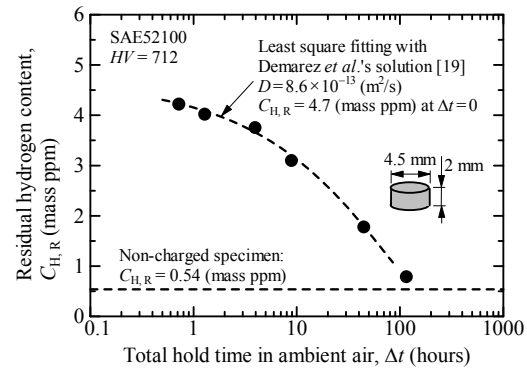

Figure 6. Residual hydrogen content as a function of total hold time in ambient air [12]

defect significantly decreased the nominal stress at the final fracture of specimen, σ_f, which was decreased with an increase in the defect size.

Table 1 lists the chemical compositions of all the inclusions at fracture origin together with a series of experimental data. The inclusion size $\sqrt{area}$ ranged from about 10 to 30 μm. The fracture processes of specimens originated from two types of inclusions, *i.e.* $Al_2O_3 \cdot (CaO)_x$ and TiN, has been reported in a separate paper [6]. Figure 8 illustrates crack initiation processes from the two kinds of nonmetallic inclusions in the non-charged and H-precharged specimens [6]. In an early stage of the fracture process from the $Al_2O_3 \cdot (CaO)_x$ type inclusion, an interfacial cracking occurs at the pole of the inclusion/matrix interface where the tensile stress becomes maximum owing to a large modulus of the inclusion. Subsequently, the complete separation of the interface between the inclusion and matrix creates a spherical-like cavity, which shifts the location of the highest tensile stress from the pole to the equator of the cavity. On the other hand, the fracture process from the TiN type inclusion is initiated by the cracking of inclusion itself. These processes for two types of inclusions take place while the overall deformation of the specimen is elastic as shown in [6].

Figure 9 [12] shows the statistics of extremes distribution of nonmetallic inclusions at the fracture origin of the H-precharged tensile specimens, where y' is the reduced variant, F is the cumulative distribution fraction and T' is the return period. The distribution of the extreme value $\sqrt{area}_{max}$ shows a good linearity and provides a justification for the use of the distribution of extremes.

In the H-precharged specimens having artificial defect, the fracture was originated from the defect. It is worth noting that there was an exception, *i.e.* the fracture of the specimen having the smallest artificial defect (*cf.* Fig. 3(a)) was not originated from the artificial defect but from a nonmetallic inclusion, though the size of the inclusion was definitely smaller than that of the artificial defect,
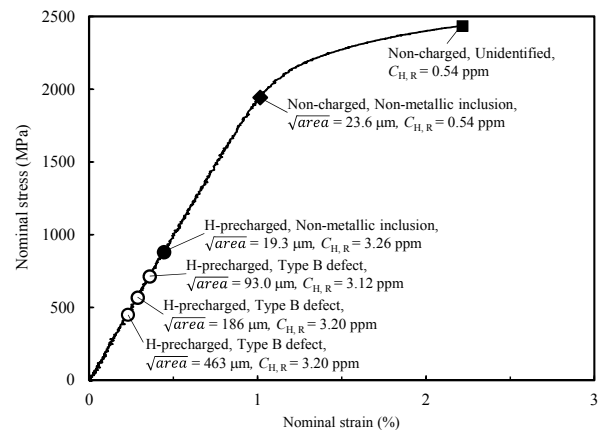

Figure 7. Example of the stress-strain curve and fracture points

as compared in Table 1 [12]. This is due to the non-uniform distribution of hydrogen concentration in the specimen from the surface to the center.

3.3 Dependence on the threshold stress intensity on defect size and hydrogen concentration

In order to quantitatively characterize the hydrogen effect together with the defect size dependence on the fracture toughness, the fracture data will be analyzed in terms of the macroscopic fracture stress σ_f, the defect size $\sqrt{area}$ and the residual hydrogen content $C_{H, R}$.

3.3.1. Smooth specimens

Firstly, we associate the fracture stress σ_f with K_{TH} for the onset of a crack from a spherical inclusion. After the interfacial debonding between inclusion and matrix, the spherical inclusion can be regarded as a traction free cavity (*cf.* Fig. 8). Figure 10 shows the normalized stress intensity factor $K_I/\sigma_0\sqrt{a'+\lambda}$ for a crack emanating from an ellipsoidal cavity as a function of the parameter λ/a',

Table 1. Experimental data of SAE52100 [12]

|	t_1 (min)	t_2 (min)	Fracture origin	$C_{H, R}$ (mass ppm)	σ_f (MPa)	$\sqrt{area}$ (μm)	K_{TH} (MPa $\sqrt{m}$)
H-precharged specimens	27	76	Al, Ca, Mg, Si, S	3.29	795	15.0	2.73
	49	111	Al, Ca, Si	3.17	785	19.3	3.06
	27	89	Ti, C	2.46	1027	11.6	3.10
	21	90	Al, Ca, Mg, Si, S	3.64	769	22.4	3.23
	45	108	Al, Ca, Mg, Si, S	3.00	897	18.8	3.45
	32	90	Al, Ca	3.79	779	25.0	3.45
	21	89	Al, Ca, Mg, Si	3.06	943	16.3	3.37
	31	94	Al, Mg	3.26	883	19.3	3.44
	47	108	Al, Ca, Mg, Si	3.08	802	23.9	3.47
	32	89	Al, Ca, P, Si	3.89	845	22.3	3.54
	25	75	Al, Ca, Mg, Si	2.95	773	27.6	3.60
	29	97	Al, Ca, Si	3.05	1001	19.8	3.95
	34	94	Al, Ca, Mg, Si	2.69	1031	19.0	3.98
	20	85	Ti, N, Mn, S	2.32	1041	19.3	4.05
	24	105	Semi-circular slit	3.12	714	93.0	7.93
	24	94	Semi-circular slit	3.20	567	186	8.90
	27	94	Semi-circular slit	3.20	450	463	11.15
	21	102	Drilled hole + FIB slits	3.39	657	116	7.28
	28	117	Drilled hole + FIB slits	3.95	668	196	10.47
	30	112	Electro discharged + FIB slits	3.77	471	513	11.67
	20	102	Al, Ca, Mg, Si, S	3.03	960	12.4*	3.00
			Rectangular FIB slit			35.0	
Non-charged specimen	—	—	Al, Ca, Mg, S	0.54	1943	23.6	8.37
	—	—	Unidentified	0.54	2436	—	—
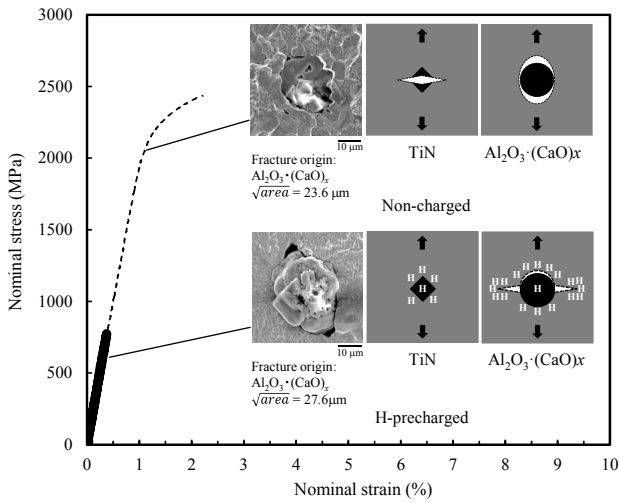
Figure 8. Illustration of crack initiation processes from two kinds of non-metallic inclusions [6]
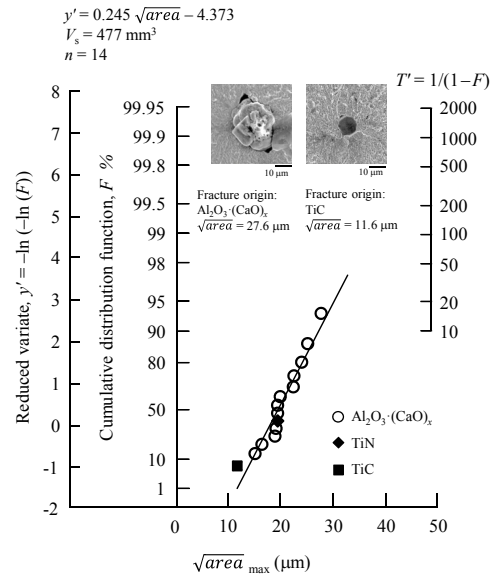

Figure 9. Statistics of extremes distribution of inclusions at the fracture origin [12]

where σ_0 is the remote tensile stress, a' is the large semi-axis of the ellipsoid and λ is the crack length measured from the equator of the ellipsoid [15]. As shown in Fig. 10, K_I for a crack with λ/a' of 0.2 is approximately equal to the stress intensity factor for a penny shaped crack with the radius of $a'+\lambda$. By considering such a steep growth in K_I value together with the presence of the interfacial cracking or cracked inclusion in the early stage of the fracture process (*cf.* Fig. 8), it can be deemed that the ellipsoidal nonmetallic inclusions are mechanically equivalent to a penny-shaped crack. Such an equivalence has experimentally been confirmed for the small fatigue cracks and defects [7, 8, 10]. Accordingly, we approximate K_{TH} in terms of σ_f and the inclusion size as follows:

$$K_{TH} = (2/\pi)\, \sigma_f \sqrt{\pi a'} \tag{1}$$

As illustrated in Fig. 8, most of the $Al_2O_3 \cdot (CaO)_x$ type inclusions yield a spherical-like cavity [6]. The shape of the cavity is determined by the inclusion shape, which is not perfectly spherical but is irregular in nature. Also in the case of the TiN type inclusion, the shape of the original crack generated
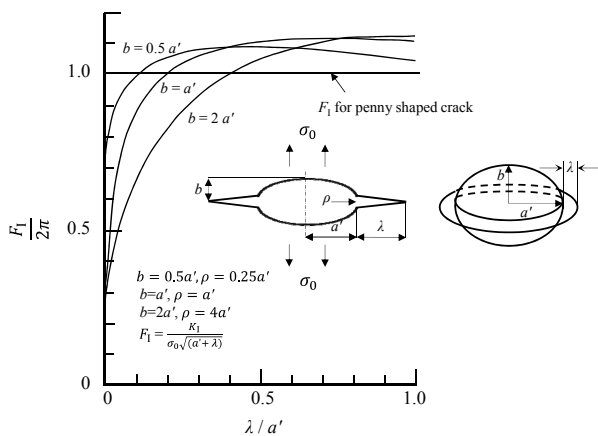

Figure 10. Normalized stress intensity factor for an annular crack emanating from an ellipsoidal cavity [15]

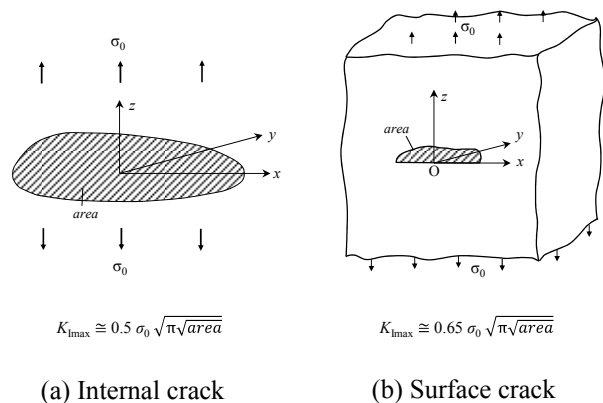(a) Internal crack   (b) Surface crack

Figure 11.   Stress intensity factor for planer cracks with arbitrary shapes [7, 8, 10]

by the cracking of inclusion itself is not circular but somewhat angular in accordance with the inclusion shape. Hence, we approximate the cracks forming at nonmetallic inclusions as planar cracks by projecting the 3-D shape of the inclusion onto the plane perpendicular to the tensile axis of the specimen [7, 8, 10]. For a planar internal crack with arbitrary shape under tension shown in Fig. 11(a), K_{Imax} along the crack front is approximately given by [7, 8, 10].

$$K_{Imax} = 0.5\sigma_0 \sqrt{\pi\sqrt{area}} \tag{2}$$

Thus, K_{TH} for H-precharged smooth specimens associated with K_{Imax} is expressed by

$$K_{TH} = 0.5\sigma_f \sqrt{\pi\sqrt{area}} \tag{3}$$

K_{TH} obtained through this equation yields a magnitude which differs from that of Eq. (1) for the perfectly penny-shaped crack by only about 4%. All the fracture data are listed in Table 1.

The primary objective in this study is to determine the initiation threshold K_{TH} for the onset of crack propagation from small cracks in components exposed to high pressure hydrogen gas. It is well known in metal fatigue that ΔK_{th} for small cracks is not a material constant; ΔK_{th} for small cracks is smaller than that for long crack [7, 8, 10, 16]. In this study, we will explore whether such a size dependence exists or not in the case of small cracks in H-precharged specimens under static loading. Figure 12 shows K_{TH} plotted respectively against the inclusion size $\sqrt{area}$ and the residual hydrogen content measured right after the final fracture of each specimen $C_{H,R}$ [12]. Regardless of some visible scatter in the experimental data in Fig. 12, one can note the following trends:
   • K_{TH}, decreases with an decrease in the inclusion size $\sqrt{area}$.
   • K_{TH}, decreases with an increase in the residual hydrogen content $C_{H,R}$.
By means of these two dominant factors, the experimental data shown in Fig. 12 can be linearly interpolated by

$$K_{TH} = 3.89 + 0.0555 \sqrt{area} - 0.494 C_{H,R} \tag{4}$$

Where, $\sqrt{area}$ is in μm and $C_{H,R}$ is in mass ppm. Figure 13 replots the data in Fig. 12 modified based on Eq. (4) [12]. Equation (4) is expressed as a linear function of $\sqrt{area}$ and $C_{H,R}$, because the variation range of these variables are small such as 10-30μm of inclusion size. However, the equation applicable to wider variation range of these variables must be reconstructed as described later.

The reason for the dependence of K_{TH} on the inclusion size is explained as follows. Recall that the distribution of tensile stress along the axis of symmetry (x direction) ahead of the crack of length $2a$ in an infinite plate under remote tensile stress σ_0 in the y direction is described by
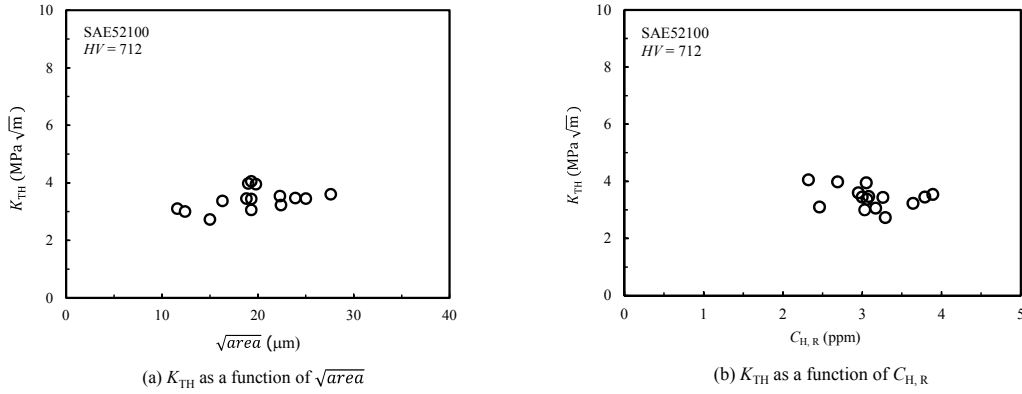
$$\sigma_{yy} = \frac{\sigma_0 x}{\sqrt{x^2 - a^2}} \tag{5}$$

(a) K_{TH} as a function of $\sqrt{area}$

(b) K_{TH} as a function of $C_{H, R}$

Figure 12. K_{TH} data plotted respectively against $\sqrt{area}$ and $C_{H, R}$ [12]
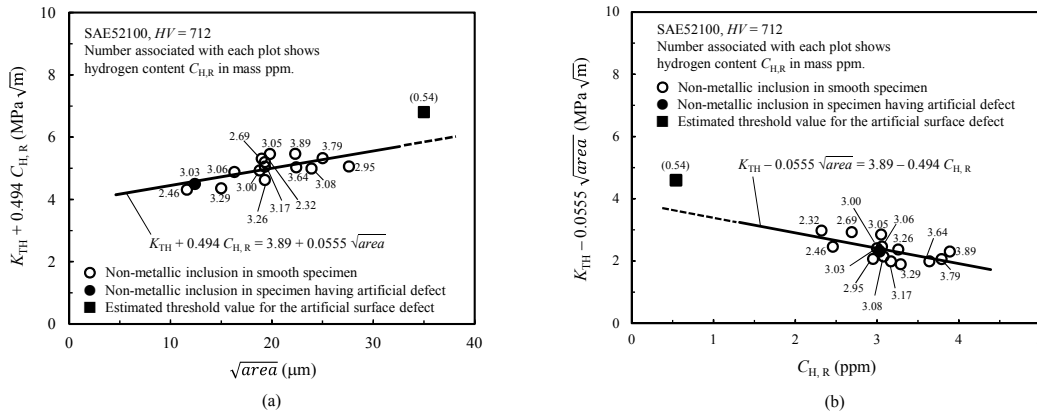

(a)

(b)

Figure 13. Threshold K_{TH} for SAE52100 expressed in terms of $\sqrt{area}$ and $C_{H, R}$ [12]

Particularly for very small distances, r, from the crack tip along the axis of symmetry, Eq. (5) yields

$$\sigma_{yy} = \frac{K_I}{\sqrt{2\pi r}} \qquad (6)$$

Where, $K_I = \sigma_0 \sqrt{\pi a}$ is the stress intensity factor. Figure 14 shows an example of the comparison of stress field ahead of the tip of two different sizes of cracks under a stress intensity factor K_I of 10 MPa$\sqrt{m}$ which were obtained by Eq. (5). In both cases, σ_0 was determined so that K_I is equal to 10 MPa$\sqrt{m}$. In the *large crack* (*e.g.* $2a = 20$ mm), the singular stress field decays very fast from the crack tip. In this case, Eq. (5) can be well represented by Eq. (6) to characterize the stress field near the crack tip. On the other hand, in the *small crack* (*e.g.* $2a = 0.02$ mm), a large discrepancy arises between the stress fields in these two cracks. Such a discrepancy in the stress field near crack tip between small crack and large crack also arises even if the material is not the perfectly elastic but the elastic-plastic. For this reason, the tensile stress field ahead of the tip of small crack cannot be determined uniquely through the stress intensity factor alone, and therefore the calculated threshold values for small cracks show a crack size dependence.

3.3.2. Specimens having artificial surface defects

For a planar cracks with arbitrary shape at specimen surface (*cf.* Fig. 11(b)), K_{Imax} along the crack front can be approximated by [7, 8, 10].

$$K_{\text{Imax}} = 0.65\sigma_0 \sqrt{\pi\sqrt{area}} \tag{7}$$

Thus, considering the mechanical equivalence between small crack and defect as discussed in the previous section, K_{TH} for surface defects associated with K_{Imax} is expressed by

$$K_{\text{TH}} = 0.65\sigma_{\text{f}} \sqrt{\pi\sqrt{area}} \tag{8}$$

Figure 15 shows the K_{TH} values both for the artificial surface defects and nonmetallic inclusions as a function of the defect size $\sqrt{area}$ [12]. The data are shown in a double logarithmic diagram, as has widely been used for the arrangement of ΔK_{th} data of the small fatigue cracks [7, 8, 10, 16]. It is well known that in fatigue crack the threshold stress intensity factor range ΔK_{th} has the following relation with the defect size in the small crack regime, *e.g.* $\sqrt{area} < 1$ mm.

$$\Delta K_{\text{th}} \propto (\sqrt{area})^{1/3} \tag{9}$$

Also in the present results for K_{TH}, we can see a definite size dependence in the range between about 10 and 500 μm in Fig. 15, *i.e.* K_{TH} was reduced with a decrease in $\sqrt{area}$. However, the exact dependence of the threshold value on the defect size is not clear at present since the threshold value can be varied also with the hydrogen concentration at the location of fracture origin, as will be discussed in the next section. As a reference data, in Fig. 15, the shaded area shows the Moody *et al.*'s K_{TH} data for a large crack in the standard CT and WOL specimens of AISI4340 steel with the yield strength σ_{YS} of 1500 ~ 1900 MPa, which was determined from tests in hydrogen gas, NaCl solutions and H-precharged specimens [4]. The values of K_{TH} for both the nonmetallic inclusions and artificial defects were definitely smaller than those for the large cracks, though the effect of some influencing factors, *e.g.* material type, strength level, hydrogen content, strain rate *etc.*, should further be clarified in the future.
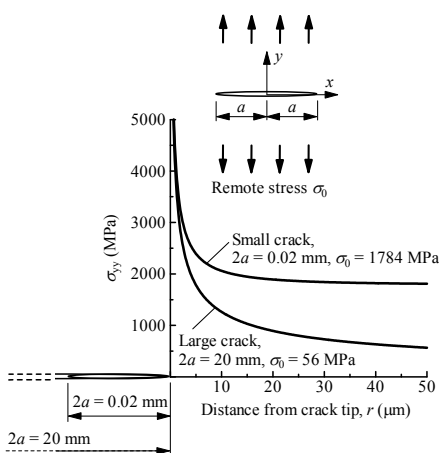

Figure 14. Comparison of stress field ahead of tip of *large* and *small* cracks under a stress intensity factor $K_{\text{I}} = 10$ MPa$\sqrt{\text{m}}$
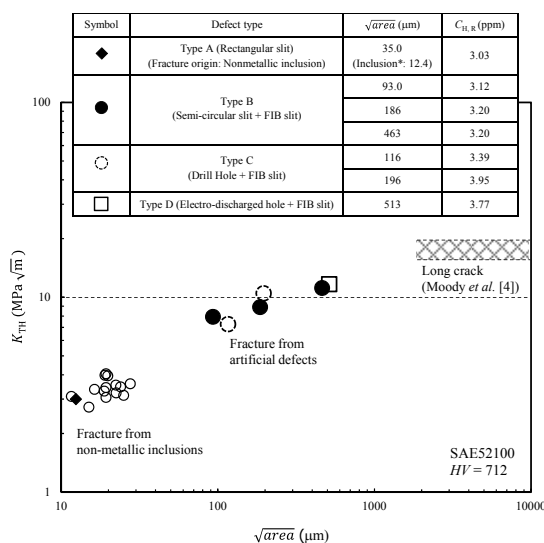

Figure 15. Relationship between K_{TH} and $\sqrt{area}$ for both short and long cracks in SAE52100. ◆: The specimen had the artificial defect, but was fractured from a non-metallic inclusion [12]

4. Conclusions

A series of uniaxial tensile tests of a H-precharged SAE52100 steel were carried out to determine the fracture toughness for the failure originated from nonmetallic inclusions and small artificial defects. The results are summarized as follows:

(1) All the H-precharged specimens failed in the elastic regime irrespective of the presence or absence of the artificial defect.

(2) In the smooth specimens, fracture origins were nonmetallic inclusions with the size of 10 ~ 30 μm (*e.g.* $Al_2O_3 \cdot (CaO)_x$, TiN and TiC).

(3) Fracture of specimens having the artificial defect with sizes of about 100 ~ 500μm were originated from the defects.

(4) The threshold intensity factor K_{TH} was decreased with a decrease in defect size in the small crack regime. The values of K_{TH} for small defects were much smaller than those for large cracks in the standard specimens such as CT and WOL. For the safer design against the fracture toughness for small cracks, the crack size dependence should be taken into consideration.

References

[1] Y. Murakami, S. Matsuoka, Y. Kondo, S. Nishimura, Mechanism of Hydrogen Embrittlement and Guide for Fatigue Design. Yokendo, Tokyo, Japan (2012).

[2] R.P. Gangloff, B.P. Somerday, Ed., Gaseous hydrogen embrittlement of materials in energy technologies, Volume 1, Woodhead publishing, Oxford, UK (2012).

[3] Y. Murakami, H. Matsunaga, International Journal of Fatigue, 28 (2006) 1509-1520.

[4] R.N. Moody, S.L. Robinson, W.M. Garrison Jr., Res Mechanica, 30 (1990) 143-206.

[5] R.O. Ritchie, M.H. Castro Cedeno, *et al.*, Metall. Trans. A, 7 (1978) 35-40.

[6] Y. Murakami, T. Kanezaki, P. Sofronis, Engng. Frac. Mech., 97 (2013) 227-243.

[7] Y. Murakami, M. Endo, Int. J. Fatigue, 7 (1994) 163-182.

[8] Y. Murakami, Metal Fatigue: Effects of Small Defects and Nonmetallic Inclusions. Elsevier Ltd., Oxford, UK (2002).

[9] T. Miyamoto *et al.*, J. Soc. Mater. Sci., Japan, 59 (2010) 916-923.

[10] Y. Murakami, M. Endo, J. Soc. Mater. Sci., Japan, 35 (1986) 911-917.

[11] S. Fujita, Y. Murakami, Metall. Mater. Trans. A, 44 (2012) 2013-2033.

[12] Y. Murakami, H. Matsunaga, A. Abyazi, Y. Fukushima, Defect size dependence on threshold stress intensity for high strength steel with internal hydrogen, submitted (2013).

[13] A. Demarez, A.G. Hocks, F.A. Meuniers, Acta Metallurgica, 2 (1954) 214-223.

[14] K.A. Nibur, *et al.* SAND2010-4633, Sandia National Lab. (2010).

[15] Y. Murakami, Ed. in chief, Stress Intensity Factors Handbook, Vol. 2. 871-873, Pergamon Press, UK (1987).

[16] H. Kitagawa, S. Takahashi, Trans. Japan Soc. Mech. Engineers, Ser. A, 45 (1979) 1289-1303.